ACS OMEGA

http://pubs.acs.org/journal/acsodf

Article

Importance of Solvent-Bridged Structures of Fluorinated Diphenylalanines: Synthesis, Detailed NMR Analysis, and Rotational Profiles of Phe(2-F)-Phe(2-F), Phe(2-F)-Phe, and Phe-Phe(2-F)

Kaidi Yang, Fabio Gallazzi, Christina Arens, and Rainer Glaser*

Cite This: *ACS Omega* 2022, 7, 42629–42643

Read Online

ACCESS | Metrics & More | Article Recommendations | Supporting Information

ABSTRACT: The crystal structure of L-phenylalanyl L-phenylalanine (Phe-Phe, FF, a.k.a. diphenylalanine) is not merely noncentrosymmetric, but it is highly dipole parallel aligned. It is for this reason that FF is a nonlinear optical (NLO) material and exhibits strong second harmonic generation (SHG). Enhancement of the SHG response by *ortho* fluorination was demonstrated. Crystallization is nontrivial, and learning about the zwitterion structures in solution is important for the rational improvement of the crystallization process. Here, we present an NMR study of difluorinated FF (Phe(2-F)-Phe(2-F)) and mono-fluorinated FF isomers (Phe(2-F)-Phe and Phe-Phe(2-F)). The dipeptides were prepared by solid-phase synthesis and purified by high-performance liquid chromatography (HPLC). Their ^{1}H and ^{13}C NMR spectra were recorded in partially deuterated water (10% D_2O), and two-dimensional (2D) NMR techniques were employed for signal assignments. The unambiguous assignments are reported of all chemical shifts for the aliphatic H and C atoms and of the C atoms of the carboxylate, the amide carbonyl, the CF carbons, and of every arene C atom in each phenyl ring. The dipeptides are *trans* amides and intramolecular hydrogen bonding between the ammonium group and the amide carbonyl restricts the $H_3N{-}CH{-}C(O)$ geometry. We explored the rotational profile of the diphenylalanines as a function of the $\tau = \angle(C{-}N{-}C{-}CO_2)$ dihedral angle at the SMD(B3LYP/6-31G*) level without and with specific hydration and report the associated Karplus curves $J(\theta)$ vs $\theta = \angle(H{-}N{-}C{-}H)$. The rotational profiles show a maximum of three stationary structures, and relative conformer stabilities of the free diphenylalanines show that the conformation found in the crystal **M1** is the least stable among the three, **M3** > **M2** ≫ **M1**. Specific water solvation makes all of the difference and adds a large competitive advantage to the water-bridged ion pair **M1a**. In fact, **M1a** becomes the most stable and dominant conformation for the parent diphenylalanine and mono1 F-FF and **M1a** becomes competitive with **M3c** for mono2 F-FF and di F-FF. Implications are discussed regarding the importance of the conformational preorganization of diphenylalanines in solution and the facility for their crystallization.

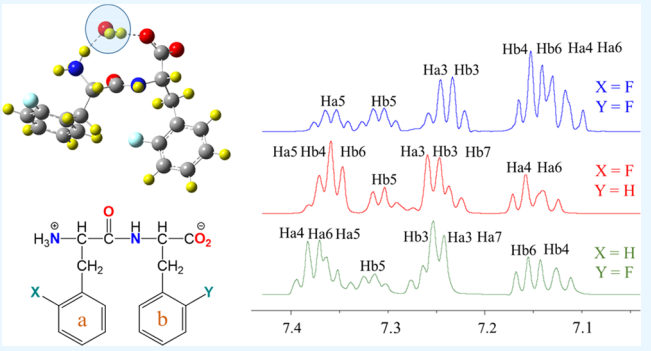

1. INTRODUCTION

Nonlinear optical (NLO) materials alter some aspect of incident light, such as the plane of polarization or the frequency,[1] and these materials are ubiquitous in daily life.[2] Second harmonic generation (SHG) is the most important property of NLO materials, that is, the phenomenon that the materials emit light with twice the frequency of the incident light.[3,4] Noncentrosymmetry is a requirement for a material to exhibit SHG activity.[5] SHG materials play essential roles in the fields of optical signal processing, optical limiting systems, parametric oscillators, and data storage.[6] Many traditional SHG materials are inorganic materials, but organic materials are becoming more important as NLO materials.[7,8] Organic NLO materials typically are based on noncentrosymmetric, conjugated donor−acceptor molecules.[9,10] Biological materials[11] peptides play an increasing role as NLO materials because the intrinsic chirality of the amino acids ensures noncentrosymmetry.[12,13]

Phenylalanyl phenylalanine (Phe-Phe, FF, a.k.a. diphenylalanine) is a zwitterion (Scheme 1) and self-assembles into nanomaterials that exhibit SHG. The crystal structure of FF is not merely chiral because of the intrinsic chirality of any amino acid, but it is highly dipole aligned.[14,15] In the crystal structure, six FF zwitterions form a helical ring around the "interior channel" and the stacking of such rings forms a nanotube.[16] The immediate environment of one FF zwitterion is shown in Scheme 1 based on the crystal structure data. Contact ion pairs are formed between neighboring FF zwitterions (green highlight

Received: October 1, 2022
Accepted: November 2, 2022
Published: November 11, 2022

Scheme 1. Stereochemistry of FF and ROH-Bridged FF

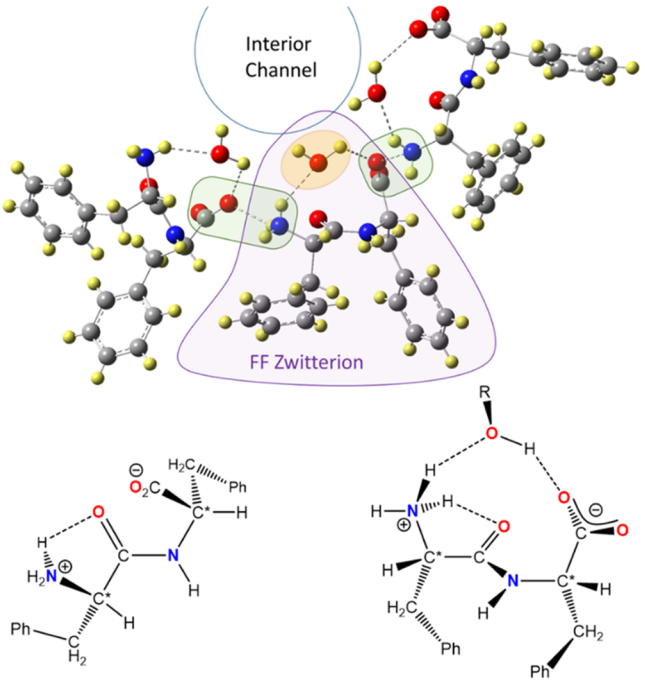

in Scheme 1). It is one of the characteristic features of the crystal structure that the interior channel contains crystal water, which stabilizes the zwitterions by the formation of the intramolecular water-separated ion pairs (orange highlight in Scheme 1). We will quantify the stabilization afforded by the formation of the water-separated ion pair. All of the carbonyl groups of the FF amide backbone are pointing in the same direction and result in the polar alignment in the entire nanotube. Diphenylalanine has been applied successfully for the fabrication of drug delivery systems,[17] optical waveguides,[18] and antibacterial agents.[19] The self-assembled FF nanotubes can be used as chiral sensing platform[20] and as molds for metal nanowires.[21] A variety of modified diphenylalanines have been studied because of the simple synthesis of FF and the ease of its chemical modification.[22−24]

We have been interested in studying the effects of fluorination on the properties of FF. We have demonstrated the successful improvement of the SHG signal intensity by replacing an *ortho* H with a fluorine atom in both benzene rings, di F-FF in Scheme 2.[25,26] To study the mechanism of this SHG enhancement, we

Scheme 2. Structures of FF, Isomers of Mono F-FF, and Di F-FF

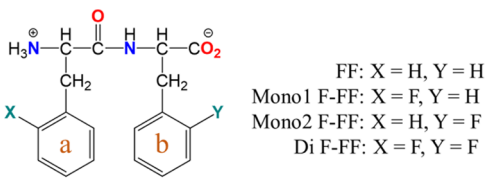

wanted to expand the scope of our study to include the mono-fluorinated FF molecules. In the present paper, we present a comparative study of di F-FF, mono1 F-FF, and mono2 F-FF (Scheme 2). Only one benzene ring is *ortho*-fluorinated in the isomers mono1 F-FF and mono2 F-FF. In mono1 F-FF (Phe(2-F)-Phe), only the benzene of the phenylalanine at the *N*-terminus is fluorinated, and in mono2 F-FF (Phe-Phe(2-F)), it is the benzene close to the *C*-terminus that is fluorinated. The dipeptides were prepared by solid-phase synthesis, and their purity and identity were established by liquid chromatography−mass spectrometry (LC−MS) analysis. A variety of one- and two-dimensional NMR spectroscopic techniques were applied to obtain complete assignments of their ^{1}H and ^{13}C NMR signals.

The presented NMR measurements in principle can discriminate between structural options in the accessible conformational space, but such mapping is not trivial because each of the diphenylalanines may occupy a vast conformational space (Scheme 1, left). However, there are a few reasonable constraints to allow a first analysis of the structural chemistry in solution. Each dipeptide will be a *trans* amide with ∠(O═C−N−H) ≈ 180° and the ammonium group will engage in hydrogen bonding with the amide carbonyl restricting the H−C−C(O)−N−H geometry. The zwitterion is a frustrated ion pair in that its ammonium group and the carboxylate group cannot approach each to form a stable contact ion pair $(H_2N-H)^+\cdots(OCO)^-$. Because of this frustration, the carboxylate will prefer a position that allows for the formation of a solvent-separated ion pair $(H_2N-H)^+\cdots O(R)-H\cdots(OCO)^-$. The bridging by water (R = H) or alcohol (R = alkyl) in the solvent-separated ion pair imposes strong constraints on the H−N−C−H geometry (Scheme 1, right). Thus, we include an extensive computational study of the rotational profiles about the N−C bonds of the parent diphenylalanine and the three fluorinated derivatives. Karplus analysis of the structures along the rotational profiles shows that the $^{3}J_{HNCH}$ coupling constants do not differentiate between possible conformations. However, the computed thermochemistry shows that the inclusion of the specific solvation is key to adequately assess the relative importance of the N−C conformations.

2. SYNTHESIS AND CHARACTERIZATION

2.1. Synthesis of Fluorinated Diphenylalanine. All three peptides were prepared manually in a reaction vessel for peptide synthesis on 2.5 g of 2-chlorotrityl (2-ClTrt) chloride resin.

2.1.1. Synthesis of Di F-FF. Fmoc-L-Phe(2-F)-OH (1.2 g, 3 mmol) were added to the resin together with 1.7 mL of *N*,*N*-diisopropylethylamine (DIPEA, 10 mmol). The reaction was left to proceed for 1 h and then repeated. Capping of the resin was then performed with MeOH (5 min, 15 mL), and the loading of the resin was experimentally shown to be ≈0.6 mmol g^{-1} by high-performance liquid chromatography (HPLC)-based quantitative Fmoc evaluation test. Fmoc deprotection was achieved by treatment with 20% piperidine in dimethylformamide (DMF) for 20 min, repeated twice.

The second protected amino acid, Fmoc-L-Phe(2-F)-OH (2.4 g, 6 mmol), was reacted with 3.4 mL of DIPEA (20 mmol) and subsequently with 2 g of 2-(1*H*-benzotriazol-1-yl)-1,1,3,3-tetramethyluronium hexafluorophosphate (HBTU) (5.5 mmol) for 5 min to provide the corresponding activated ester. This activated ester was reacted in situ with the peptidyl resin for 1 h. The same coupling procedure was repeated once to afford the protected dipeptide on the resin. Capping of unreacted amino groups of the first phenylalanine residue by acylation was achieved by reaction with 5% Ac_2O and DIPEA for 5 min. Final Fmoc deprotection was performed as above to obtain the desired dipeptide on the resin.

Acid-catalyzed ester hydrolysis was used to cleave the peptide from the resin and involved treatment with 10% trifluoroacetic

https://doi.org/10.1021/acsomega.2c06351
ACS Omega 2022, 7, 42629−42643

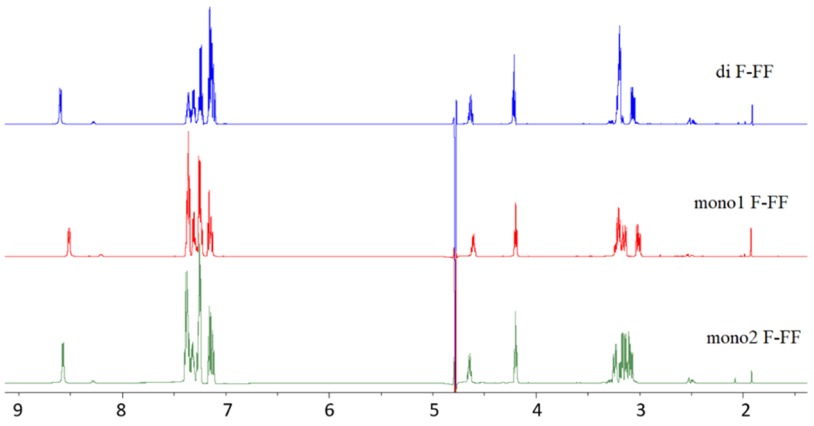

Figure 1. Measured ^{1}H NMR spectra of di F-FF, mono1 F-FF, and mono2 F-FF.

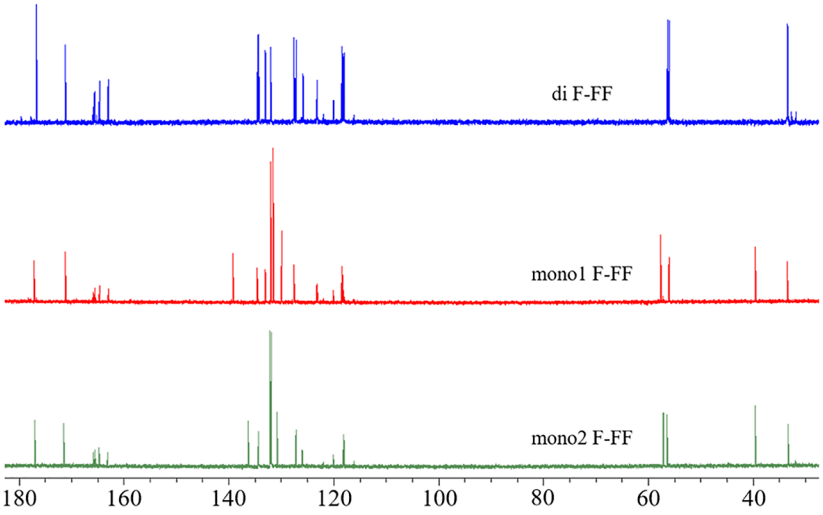

Figure 2. Measured ^{13}C NMR spectra of di F-FF, mono1 F-FF, and mono2 F-FF.

acid (TFA) in the presence of water and triisopropylsilane (TIPS) scavengers (both 5%) in dichloromethane (DCM). After 45 min of reaction, the reaction mixture was filtered and evaporated by nitrogen to almost dryness before being diluted with 50% water and acetonitrile and lyophilized overnight to obtain 500 mg of crude dipeptide. Crude dipeptide identity was confirmed by LC−MS analysis, and its preparative purification by MS-assisted flash chromatography yielded 158 mg of 93% pure H_2N-Phe(2-F)-Phe(2-F)-COOH.

2.1.2. Synthesis of Mono F-FF. The syntheses of both mono1 and mono2 F-FF were performed in complete analogy to the procedure described for di F-FF and details are provided in the Supporting Information.

2.1.3. LC−MS Analysis of Dipeptides. The purity and identity of each dipeptide were established by LC−MS analysis. In the Supporting Information, we provide the LC chromatogram and the electrospray ionization (ESI) mass spectrum for each dipeptide. The molecular ions appear at m/z = 348.97 (di F-FF) and at m/z = 331 (mono F-FF).

2.2. NMR Measurements of Fluorinated Diphenylalanine. NMR data of the F-FF molecules were collected on a Bruker 600 MHz NMR spectrometer. All measurements were performed in partially deuterated water (10% D_2O and 90% H_2O). ^{1}H NMR chemical shifts δ are reported in ppm relative to TMS and data in parentheses lists the signal multiplicity (d = doublet, t = triplet, q = quartet, and m = multiplet), integrated signal intensity in H equivalents, and coupling constant information. ^{13}C NMR chemical shifts δ are reported in ppm relative to TMS. ^{19}F NMR chemical shifts δ are reported in ppm relative to $CFCl_3$, and the internal standard trifluoroacetic acid was used and set to δ = −76.50 ppm and data in parentheses lists the signal multiplicity and assignment. Several two-dimensional NMR techniques were employed, and these include total correlation spectroscopy (TOCSY), heteronuclear single-quantum correlation spectroscopy (HSQC), heteronuclear multibond correlation spectroscopy (HMBC), and nuclear Overhauser effect spectroscopy (NOESY). H−H TOCSY cross-terms inform about three-bond coupling between hydrogens.[27] C−H HSQC detects correlation between carbons directly attached hydrogens,[28] and C−H HMBC gives signals for carbons and hydrogens that are separated by two to four bonds.[29] H−H NOESY informs about hydrogen−hydrogen interactions through space.[30]

The experimental ^{1}H and ^{13}C NMR spectra, respectively, of di F-FF, mono1 F-FF, and mono2 F-FF are shown in Figures 1 and 2, respectively. The experimental ^{19}F NMR spectra are shown in Figures S6, S12, and S18. We measured many 2D-NMR spectra, and they are only provided in the Supporting Information. There are two quartet signals caused by the TFA impurity at about 166 and 120 ppm with the coupling constant being 35 and 292.1 Hz, respectively.

https://doi.org/10.1021/acsomega.2c06351
ACS Omega 2022, 7, 42629−42643

2.3. Computational Methods. Potential energy surface analyses were performed at the SMD(B3LYP/6-31G*) level, that is, the B3LYP/6-31G* theoretical level[31] was employed in conjunction with the Universal Solvation Model (SMD),[32] which we have employed successfully in the context of heterocyclic chemistry for an extensive range of solvent.[33,34] NMR spin−spin coupling constants were computed at the SMD(B3LYP/6-31G*) level and the SMD(B3LYP/6-311+G-(2d,p)) level[35] with the gauge-independent atomic orbital (GIAO) method.[36,37] In addition, the minima **M1** and **M1a** were also optimized at the MP2/6-31G* level.[38,39] The calculations were performed with Gaussian 16, Revision A.03.[40]

For each minimum optimized with B3LYP, we report in Table S1 the total energy (E, in au), vibrational zero-point energy (VZPE, in kcal mol^{-1}), thermal energy (TE, in kcal mol^{-1}), and molecular entropies S (total entropy S_{tot} and translational entropy S_{trans}, in cal mol^{-1} K^{-1}). Both Gibbs free energy ΔG and Helmholtz free energy ΔA are reported to describe the reaction thermochemistry. Because $\Delta G = \Delta A + \Delta(pV)$ and the water binding reaction is taking place in condensed phase where $\Delta(pV) \approx 0$, the ΔA value is a better estimate for the reaction energy.

In addition, the Wertz[41] correction in eq 1 estimates the translational entropy of condensed phase systems based on their gas phase entropies.

$$^{w}S_{trans} = 0.54S_{trans} + 6.578 \quad (1)$$

We apply this correction to the calculated translational entropy for each molecule because the translational component is the most affected by the transition from gas phase to solution. The Wertz-corrected Helmholtz free energy $\Delta^{w}A = \Delta H - T\cdot{}^{w}S_{tot}$ values are our best estimation to describe the reaction thermochemistry. For each minimum optimized with MP2, we report in Table S2 the same thermochemistry data.

3. ANALYSIS OF THE ALIPHATIC REGIONS OF THE NMR SPECTRA

3.1. Atom Labeling and Complete Assignments of H NMR and C NMR. The labeling of the H and C atoms is shown in Scheme 3. The Phe group that is close to the NH_3^+ end of FF is labeled as *a* part and the Phe group that is close to the COO^- end is labeled as *b* part, respectively.

Scheme 3. Labeling of F-FF Used for the NMR Assignment

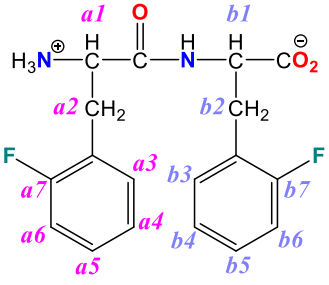

The complete assignment of every NMR signal is shown in Table 1 for H NMR and F NMR spectra and Table 2 for C NMR spectra. These assignments will be justified below.

The standard report of NMR assignments is shown below. All coupling constants refer to $^{3}J_{H-H}$ unless specified otherwise. The NMR calculations show that J_{H-F} coupling constants are positive except for $^{5}J_{H4-F}$, which is negative and very small in magnitude. We measured the three J_{C-F} coupling constants $^{2}J_{C6-F}$, $^{1}J_{C7-F}$, and $^{2}J_{C8-F}$, and NMR calculations show that the $^{1}J_{C7-F}$ values are negative, while the others are positive.

3.1.1. Di F-FF. ^{1}H NMR: δ_H 8.60 (0.8H, d, J = 7.6 Hz, NH), 7.36 (1H, ddd, $J_1 \approx J_2 \approx {}^{4}J_{3(H-F)}$ = 7.3 Hz, Ha5), 7.31 (1H, ddd, $J_1 \approx J_2 \approx {}^{4}J_{3(H-F)}$ = 6.9 Hz, Hb5), 7.24 (2H, m, Ha3 and Hb3), 7.09−7.16 (4H, m, Ha4, Hb4, Ha6, and Hb6), 4.62 (1H, ddd, $J_1 \approx J_2 \approx J_3$ = 7.5 Hz, Hb1), 4.21 (1H, dd, $J_1 \approx J_2$ = 7.1 Hz, Ha1), 3.16−3.22 (3H, m, Ha2, Ha2′, and Hb2′), 3.04−3.08 (1H, dd, ^{2}J = 13.7 Hz, J = 7.9, Hb2).

^{13}C NMR: δ_C 33.3 (Ca2 and Cb2), 55.9 (Ca1), 56.2 (Cb1), 118.0 (1C, d, $^{2}J_{C-F}$ = 21.6 Hz, Ca6), 118.2 (1C, d, $^{2}J_{C-F}$ = 21.6 Hz, Cb6), 123.1 (1C, d, $^{2}J_{C-F}$ = 15.8 Hz, Ca8), 125.6 (1C, d, $^{2}J_{C-F}$ = 15.8 Hz, Cb8), 127.1 (Ca4), 127.4 (Cb4), 131.9 (Cb5), 132.95 (Ca5), 134.2 (Cb3), 134.4 (Ca3), 163.82 (2C, d, $^{1}J_{C-F}$ = 243.1 Hz, Ca7 and Cb7), 171.1 (C═O), 176.62 (COO^-).

^{19}F NMR: δ_F −119.28 (1F, m, Fb), −118.93 (1F, m, Fa).

3.1.2. Mono1 F-FF. ^{1}H NMR: δ_H 8.51 (0.8H, d, J = 7.7 Hz, NH), 7.35 (3H, m, J = 7.0 Hz, Ha5, Hb4, and Hb6), 7.27−7.31 (1H, m, Hb5), 7.22−7.25 (3H, m, Ha3, Hb3, and H7), 7.16 (1H, dd, $J_1 \approx J_2$ = 7.9 Hz, Ha4), 7.15 (1H, d, J = 9.4 Hz, Ha6), 4.60 (0.7H, ddd, $J_1 \approx J_2 \approx J_3$ = 7.3 Hz, Hb1), 4.19 (1H, dd, $J_1 \approx J_2$ = 6.9 Hz, Ha1), 3.12−3.23 (3H, m, Hb2, Ha2, and Ha2′), 3.01 (1H, dd, $^{2}J_1$ = 14.0 Hz, J_2 = 8.1 Hz, Hb2n).

^{13}C NMR: δ_C 33.3 (Ca2), 39.4 (Hb2), 55.9 (Ca1), 57.5 (Cb1), 118.2 (1C, d, $^{2}J_{C-F}$ = 21.6 Hz, Ca6), 123.1 (1C, $^{2}J_{C-F}$ = 15.6 Hz, Ca8), 127.5 (Ca3), 129.8 (Cb5), 131.4 (Cb3 and Cb7), 131.9 (Cb4 and Cb6), 134.5 (Ca5), 139.1 (Cb8), 163.7 (d, $^{1}J_{C-F}$ = 243.9 Hz, Ca7), 171.1 (C═O), 177.08 (COO^-).

^{19}F NMR: δ_F −118.88 (1F, m, Fa).

3.1.3. Mono2 F-FF. ^{1}H NMR: δ_H 8.57 (0.8H, d, J = 7.4 Hz, NH), 7.33−7.39 (3H, m, Ha4, Ha6, and Ha5), 7.31 (1H, m, Hb5), 7.24−7.27 (3H, m, Hb3, Ha3, and H7), 7.11−7.16 (2H, m, Hb6 and Hb4), 4.64 (0.7H, ddd, $J_1 \approx J_2 \approx J_3$ = 7.2 Hz, Hb1), 4.19 (1H, dd, $J_1 \approx J_2$ = 7.0 Hz, Ha1), 3.22−3.25 (1H, m, ^{2}J = 14.1 Hz, J = 6.4 Hz, Hb2), 3.06−3.19 (3H, m, Ha2, Ha2′, and Hb2′).

^{13}C NMR: δ_C 33.2 (Cb2), 39.5 (Ca2), 56.3 (Cb1), 57.0 (Ca1), 118.0 (d, 1C, $^{2}J_{C-F}$ = 21.65 Hz, Cb6), 123.13 (d, $^{2}J_{C-F}$ = 15.8 Hz, Cb8), 127.1 (Cb4), 130.7 (Ca5), 131.8 (Ca3 and Ca7), 131.9 (Cb5) 132.0 (Ca4 and Ca6), 134.3 (Cb3), 139.17 (Ha8), 163.8 (d, $^{1}J_{C-F}$ = 243.5 Hz, Cb7), 171.4 (C═O), 176.9 (COO^-).

^{19}F NMR: δ_F −119.25 (1F, m, Fb).

3.2. Analysis of the Dipeptide Backbone: Sequence. The ^{1}H NMR spectra of the three compounds are shown in Figure 1. For all three diphenylalanine, the peak with the chemical shift at about 8.5 ppm is the amide NH signal, and it gives rise to a doublet because of coupling to the proximate CH hydrogen. The ammonium hydrogens do not show up in the spectra as expected because of their fast exchange with water. The chemical shifts of the NH hydrogens in di F-FF and mono2 F-FF are virtually the same (fluorinated *b*-phenyl) while the chemical shift in mono1 F-FF is slightly lower (nonfluorinated *b*-phenyl).

In di F-FF, the peaks of the two backbone CH hydrogens show up in the range of 4.0−4.7 ppm, and this expanded region is shown in Figure 3a. Both CH hydrogens couple to the adjacent diastereotopic methylene hydrogens and the CH hydrogen of the *C*-terminal amino acid (*b*-CH) also couples to the amide NH. The CH hydrogen that is more upfield is assigned to the *a*-CH hydrogen and gives rise to a triplet-like signal because the coupling constants with the methylene Hs are

https://doi.org/10.1021/acsomega.2c06351
ACS Omega 2022, 7, 42629−42643

Table 1. ^{1}H NMR and ^{19}F NMR Chemical Shifts (in ppm) of Fluorinated Diphenylalanines

molecules	Ha1	Ha2	Ha2′	Ha3	Ha4	Ha5	Ha6	NH	Fa
Di F_FF	4.21	3.19	3.19	7.24	7.12	7.36	7.15	8.59	−118.93
Mono1 F_FF	4.19	3.20	3.20	7.24	7.16	7.35	7.15	8.51	−118.88
Mono2 F_FF	4.19	3.15	3.50	7.24	7.35	7.24	7.37	8.57	
	Hb1	Hb2	Hb2′(n)	Hb3	Hb4	Hb5	Hb6	H7	Fb
Di F_FF	4.62	3.06	3.17	7.24	7.14	7.31	7.16		−119.28
Mono1 F_FF	4.60	3.14	3.01	7.24	7.35	7.30	7.35	7.24	
Mono2 F_FF	4.64	3.24	3.08	7.15	7.12	7.31	7.26	7.37	−119.25

Table 2. ^{13}C NMR Chemical Shifts (in ppm) of Fluorinated Diphenylalanines

molecules	Ca1	Ca2	Ca3	Ca4	Ca5	Ca6	Ca7	Ca8	C=O
Di F_FF	55.9	33.3	118.2	118.0	132.9	134.4	163.0	123.1	171.1
Mono1 F_FF	55.9	33.3	127.5	132.9	134.5	118.2	163.7	123.1	171.1
Mono2 F_FF	57.0	39.5	131.8	132.0	130.7	132.0	131.8	136.2	171.4
	Cb1	Cb2	Cb3	Cb4	Cb5	Cb6	Cb7	Cb8	COO^{-}
Di F_FF	56.2	33.3	127.4	127.1	131.9	134.2	164.5	125.6	176.6
Mono1 F_FF	57.5	39.4	131.4	131.9	129.8	131.9	131.4	139.1	177.0
Mono2 F_FF	56.3	33.2	127.1	118.0	131.9	134.3	163.8	125.8	176.9

very similar ($J \approx 7.1$ Hz). The downfield CH hydrogen is assigned to the *b*-CH hydrogen and gives rise to a quartet-like pattern for the *ddd* system. The distances between the four peaks of this "quartet" are 7.1, 7.5, and 7.7 Hz, respectively, and close examination of the peak shapes shows shoulders. This multiplet is defined by three coupling constants between Hb1 with the amide NH ($J_1 = 7.7$ Hz) and with the two methylene hydrogens Hb2 (J_2) and Hb2′ (J_3). The J_1 value was determined from the NH signal and the J_2 and J_3 values cannot be extracted by analysis of this multiplet.

The centers of the Ha1 signals in mono1 F-FF (4.19 ppm) and mono2 F-FF (4.19 ppm) both appear at slightly lower chemical shifts compared to di F-FF (4.21 ppm). In contrast, the center between the major peaks of the Hb1 signal in mono1 F-FF (4.60 ppm) appears at a slightly lower chemical shift compared to di F-FF (4.62 ppm), whereas the center of the Hb1 signal in mono2 F-FF (4.64 ppm) is shifted in the opposite direction. Phenyl fluorination is expected to increase the chemical shifts of the methylene hydrogens because of inductive effects. The absence of fluorine in the *b* moiety of mono1 F-FF explains the lower chemical shift of Hb1 compared to di F-FF. Following this simple logic, one may expect δ(Ha1, mono2 F-FF) < δ(Ha1, di F-FF), while the signals of the fluorinated moieties should be about the same; δ(Hb1, mono2 F-FF) ≈ δ(Hb1, di F-FF) and δ(Ha1, mono1 F-FF) ≈ δ(Ha1, di F-FF). Clearly, these chemical shifts are not governed by fluorination alone, but also reflect changes in the relative orientation of the phenyl groups.

The splitting patterns of the CH hydrogens in the mono F-FF molecules are very similar to those of di F-FF. The *a*-CH hydrogen couples with the two diastereotopic methylene hydrogens and give rise to a triplet-like signal. Assuming that the coupling constants are very similar, we find $J \approx 6.9$ Hz (mono1) and $J \approx 7.0$ Hz (mono2). As with the *b*-CH hydrogen signal of di F-FF, we can only determine the one coupling constant with the amide NH; $J_{NH-CH} = 7.3$ Hz in mono1 F-FF and $J_{NH-CH} = 7.2$ Hz in mono2 F-FF.

3.3. Assignment and Splitting Analysis of the Methylene Region in ^{1}H NMR Spectra. The assignment of the remaining NMR signals was performed with the help of 2D-NMR spectroscopy. The assignments of the methylene Hs shown in Figure 3b were made based on the TOCSY spectra (Figures S7, S13, and S19). For example, the CH hydrogen that is correlated to the amide NH signal in the TOCSY spectrum was assigned to the Hb1 atom. The CH_2 hydrogen signals that are correlated to Hb1 were assigned as the Hb2 and Hb2′ methylene hydrogens.

Each CH_2 group should give rise to two doublets of doublets (dd) in the H NMR spectra because of the proximity of the chiral centers. As shown in Figure 3b, one CH_2 hydrogen gives rise to a clear *dd* splitting pattern without overlap; Hb2′ in di F-FF, Hb2n in mono1 F-FF, and Hb2 in mono2 F-FF. These signals allowed for the extraction of the two coupling constants $^{2}J_{H-H}$ and $^{3}J_{CH2-CH}$ listed above. The two hydrogens from *a*-CH_2 have similar chemical shifts and thus form a broad multiplet, which appears at about 3.2 ppm for di F-FF and mono1 F-FF, and more upfield for mono2 F-FF. That is because *a*-CH_2 is attached to a fluorinated phenyl ring in di F-FF and mono1 F-FF, and to a nonfluorinated phenyl ring in mono2 F-FF. The two *a*-CH_2 hydrogens signals are too close to distinguish, so they are labeled as Ha2 and Ha2′ and assigned the same chemical shifts as shown in Table 1.

The two *b*-CH_2 hydrogens afford very different peaks: one is always significantly more downfield than the other in all three FF compounds. In both mono F-FF, the more upfield hydrogen has a stronger NOESY signal with the backbone amide H, indicating this *b*-CH_2 hydrogen's close proximity to the amide NH group. This hydrogen is labeled as Hb2n in Table 1. In di F-FF, one *b*-CH_2 hydrogen signal is overlapping with the two *a*-CH_2 hydrogen signals, making it impossible to compare the intensities of the NOESY cross-peaks between the two *b*-CH_2 signals and the NH signals. So these CH_2 hydrogens are labeled as Hb2 and Hb2′ without differentiating them.

3.4. Chemical Shift Analysis of the Aliphatic Region in ^{13}C NMR Spectra. The full ^{13}C NMR spectra of the three compounds are shown in Figure 2. The aliphatic C atoms were assigned according to the HSQC spectra (Figures S8, S14, and S20), and the results are shown in Table 2.

The peaks of the two CH_2 carbons appear in the range of 30−40 ppm. All of the carbon signals of the methylene groups attached to a fluorinated phenyl ring appear at about 33.3 ppm. In the mono F-FF, the methylene groups attached to the

https://doi.org/10.1021/acsomega.2c06351
ACS Omega 2022, 7, 42629−42643

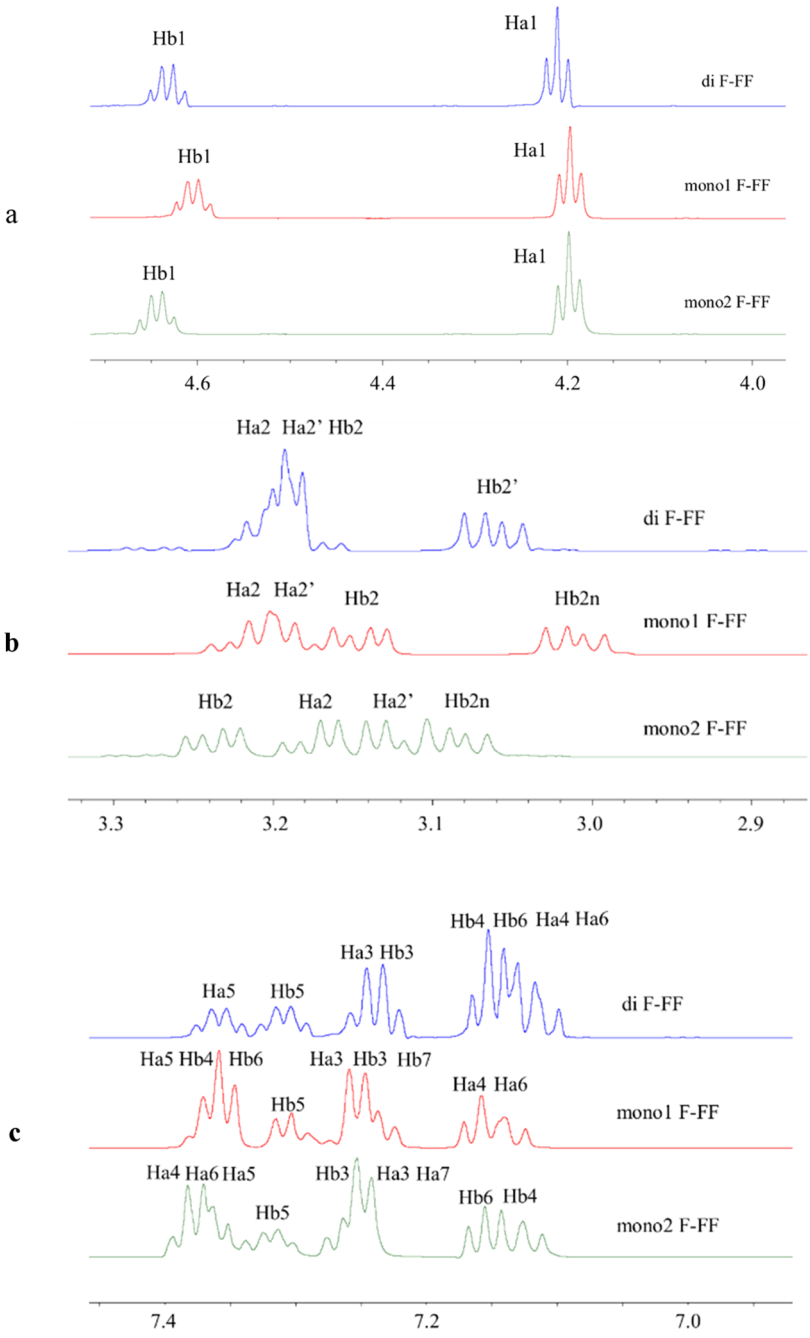

Figure 3. ^{1}H NMR spectra of di F-FF, mono1 F-FF, and mono2 F-FF. (a) Expanded backbone CH region. (b) Expanded methylene region. (c) Expanded aromatic region.

nonfluorinated phenyl ring appear at higher chemical shifts of about 39.5 ppm. The two CH carbons show up at about 56 ppm, and in mono F-FF, the CH carbon of the fluorinated Phe caused the signals that are slightly more upfield.

In all three compounds, the two most downfield peaks are carbonyl carbon signals (177 ppm for carboxylate carbon and 171 ppm for amide-C).

4. ANALYSIS OF THE AROMATIC REGIONS OF THE NMR SPECTRA

In the following discussion, we refer to the benzene positions just as in nonfluorinated diphenylalanine. Therefore, the arene C attached to the methylene group is the *ipso* carbon and fluorination occurs in the *ortho* position.

4.1. ^{1}H NMR Assignment and Splitting Analysis of the Aromatic Region. The assignments of the aromatic Hs are much more difficult because there are overlapping signals in the H NMR spectra (Figure 3c). We first identified the two *ipso* carbons according to the HSQC spectra (Figures S8, S14, and S20) and then used the HMBC spectra (Figures S9, S15, and S21) to classify the H signals into the two benzene rings. For example, the *ipso*-C in benzene *a* has an HMBC signal with the peak at 7.23 ppm in di F-FF, so we assigned that signal to Ha4. The Ca4 signal was then identified easily with the help of the HSQC spectrum. The H signal that is correlated with the *a*-CH_2 carbon in the HMBC spectrum is assigned as the *ortho* H (Ha3). And the remaining aromatic Hs in benzene *a* were assigned based on their H−H TOCSY signals with Ha4 and Ha3,

https://doi.org/10.1021/acsomega.2c06351
ACS Omega 2022, 7, 42629−42643

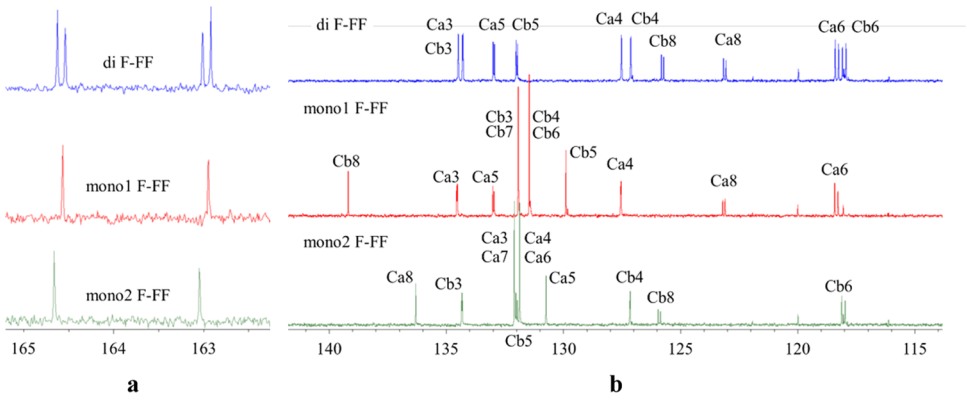

Figure 4. Expanded aromatic region of measured ^{13}C NMR spectra of di F-FF, mono1 F-FF, and mono2 F-FF: (a) Fluorinated carbons. (b) Nonfluorinated carbons.

respectively, and their H−C HMBC cross-peaks with Ca4 and Ca3, respectively.

In di F-FF, the two most downfield signal groups are caused by the *para* H atoms. Each *para* H5 couples with the two neighboring H4 and H6 atoms and shows long-range coupling with the *ortho* F atom. The value of $^4J_{H-F}$ (about 5 Hz) is usually larger than $^4J_{H-H}$ (2−3 Hz),[42] so it is more important to consider the coupling between H5 and F than between H5 and H3. The presence of fluorine strongly suggested that $^3J_{H5\text{-}H4}$ and $^3J_{H5\text{-}H6}$ would be different. Therefore, we expected a *ddd* splitting pattern for each H5 signal, which would yield the J_1, J_2, and J_3 coupling constants using the standard analysis of the *ddd* system.[43] To our surprise, however, a quartet-like pattern is observed, which indicates that $^3J_{H5\text{-}H4} \approx {}^3J_{H5\text{-}H6} \approx {}^4J_{H5\text{-}F}$ (cf., CH splitting pattern in Section 3.2).

The quartet-like signal in the center of the aromatic region is due to the H3 hydrogens. Each H3 signal is expected to cause a *dd* pattern because of coupling with H4 and F, but the signal actually presents as a false triplet ($^3J_{H3-H4} \approx {}^4J_{H3-F}$). The observed quartet-like signal group results from the overlap of the two false triplets caused by H3a and H3b, respectively. The distinction between Ha3 and Hb3 is not possible. The chemical shifts at the maximum of any overlapping peak do not inform about the precise chemical shifts of the underlying bands and, hence, there are limits to the accuracy of the extracted J values. For the four *meta* Hs, we expect a *dd* pattern for each H4 atom and each H6 atom. As can be seen in Figure 3c, the resulting signals from both benzene rings overlap in a nontractable manner.

In mono F-FFs, the presence of fluorine in only one of the benzene rings causes one additional signal for H7 and major shifts of the *meta* H4 and *meta* H6 signals in the nonfluorinated benzene. The chemical shift of the new H7 signal should be the same as for the H3 signal and the spectra of mono1 F-FF and mono2 F-FF show H7 to overlap with the H3 region. In mono1 F-FF, the most downfield signal contains *para* H from *a*-Ph^F (Ha5) as expected. The Ha5 signal overlaps with the two *meta* Hs from *b*-Ph, Hb4, and Hb6. In fluorinated benzene, the most electron-deficient centers are C7 (*ipso* relative to F) and C3 and C5 (*meta* relative to F). The *meta* Hs (H4, H6) are the most electron-rich positions because they are *ortho* or *para* relative to the fluorine and benefit from the charge alternation caused by the fluorine substituent.[44] In the *b*-Ph of mono1 F-FF, the *meta* Hs no longer benefit from that charge alternation, they are less shielded and their peaks appear more downfield. The assignment of δ(H4, H6) > δ(H5) is in agreement with the published NMR spectrum of nonfluorinated phenylalanine.[45] The most downfield multiplet signal contains one *ddd* signal from Ha5 and two *dd* signals from Hb4 and Hb6. The complexity of the signal group does not even allow the extraction of precise chemical shifts.

The second most downfield signal group is due to the *para* H from *b*-Ph (Hb5). The chemical shift of Hb5 is very similar irrespective as to whether the ring is fluorinated (di F-FF, mono2 F-FF) or nonfluorinated (mono1 F-FF). We did not expect this outcome and we cannot offer an explanation either. The Hb5 hydrogen should be coupled with the two neighboring *meta* Hs and should form a triplet if the *meta* hydrogens (H4 and H6) are magnetically equivalent. We do not observe a triplet and therefore must conclude that the *meta* hydrogens are not equivalent, possibly because of arene-arene interactions. The peaks in the region of 7.20 < δ < 7.28 ppm contain three *ortho* Hs. In fluorinated benzene, Ha3 should give rise to one *dd* signal, and in a simple benzyl derivative, Hb3 and Hb7 should afford one doublet. The complicated multiplet structure of that region again indicates intramolecular arene-arene interactions.

In mono2 F-FF, the most downfield signals are due to the *para* H and the two *meta* Hs from the nonfluorinated *a*-Ph. The two *meta* Hs move downfield because they are more electron-poor in the nonfluorinated benzene, just like with the *b*-Ph in mono1 F-FF. The two *meta* Hs should show two *dd* signals and the *para* H should show one triplet signal, and all of these peaks are overlapping. The second most downfield multiplet is caused by the *para* H in *b*-Ph. The signals in the two upfield regions are analogous to mono1 F-FF. Instead of *ortho* hydrogens Ha3, Hb3 and Hb7 in mono1 F-FF, there is now a similar multiplet due to Hb3, Ha3, and Ha7 in mono2 F-FF. Instead of *meta* hydrogens Ha4 and Ha6 in mono1 F-FF, there is now a similar multiplet due to Hb4 and Hb6 in mono2 F-FF.

4.2. ^{13}C NMR Assignments of the Aromatic Region.

There are really two aromatic regions in the carbon spectra: the region that contains fluorinated carbons (Figure 4a) and the region of the nonfluorinated carbons (Figure 4b).

The peak at about 165 ppm is due to the aromatic carbon that is attached to the F atom and the signal is split by ^{19}F (spin 1/2) to doublets with $^1J_{C-F} \approx 243$ Hz, which agrees with the reported $^1J_{C\text{-}F}$ in 2-fluoro-DL-phenylalanine.[46] In mono F-FF, there is only one fluorinated carbon and it gives rise to one doublet (J = 242.9 Hz in mono1 F-FF and J = 242.2 Hz in mono2 F-FF). In di F-FF, however, there are two fluorinated carbons, giving rise to two overlapping doublets. Comparison of the distances between the four peaks confirms that the first and the third peaks belong to

https://doi.org/10.1021/acsomega.2c06351
ACS Omega 2022, 7, 42629−42643

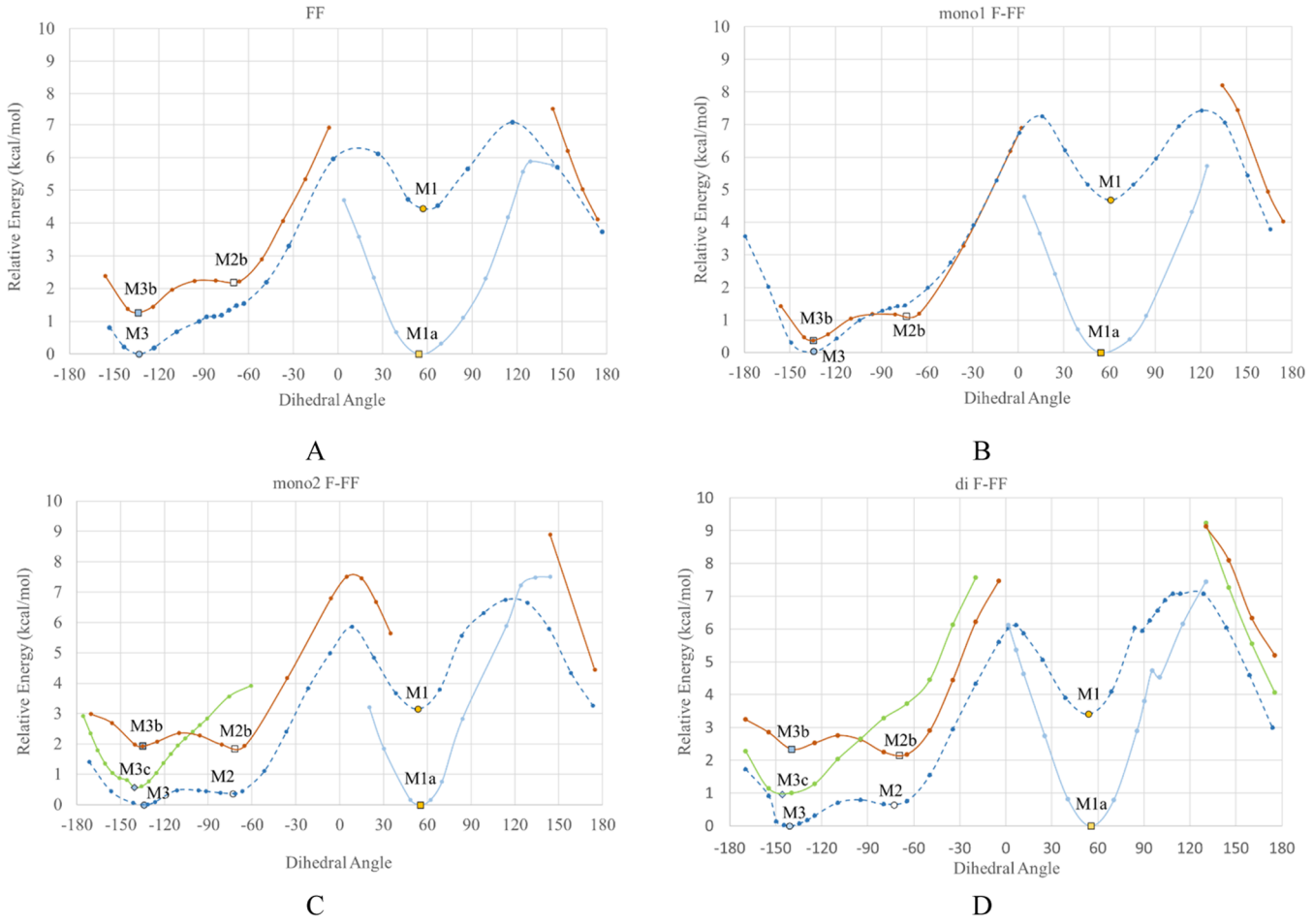

Figure 5. Rotational profiles for FF (A), mono1 F-FF (B), mono2 F-FF (C), and di F-FF (D) without and with water bridging computed at the SMD(B3LYP/6-31G*) level. In each case, the rotational profile computed without specific water solvation is shown as the dark blue dashed line. The rotational profile with specific solvation is more complicated because of varying modes of specific solvation and all parts of the profiles are shown in solid lines. See texts for details.

one doublet and the second and the fourth peaks belong to the other. Furthermore, the chemical shift and coupling constant of the more downfield di F-FF carbon signal (δ = 163.82 ppm, J = 242.5 Hz) are very similar to mono2 F-FF carbon signal (δ = 163.85 ppm, J = 242.2 Hz). And the characteristics of the more upfield di F-FF carbon signal (δ = 163.73 ppm, J = 243.0 Hz) are very close to the respective values of mono1 F-FF (δ = 163.75 ppm, J = 242.9 Hz). Thus, it can be concluded that the more downfield signal is due to C7b and the more upfield signal is due to C7a in di F-FF.

The signals of the nonfluorinated aromatic carbons show up in the range of 115 and 165 ppm. In a fluorinated benzene ring, the most upfield peaks should be expected for the *ipso* carbon (C8) and the *meta* carbons (C4 and C6) because these positions are *meta* and *para* relative to the F substituent and therefore most shielded. In the di F-FF NMR spectrum, the most upfield aromatic signals are caused by two C6, followed by two C8 and two C4. Both the C8 and C6 signals are split by the neighboring F atoms with $^{2}J_{C-F}$ coupling constants of approximately 15.7 Hz and 21.6 Hz, respectively, in agreement with the reported NMR data of fluorinated phenylalanine.[45] Compared to di F-FF, the *ipso* and *meta* carbon in the nonfluorinated phenyl ring of mono F-FF would be less shielded, thus more downfield. And that is why the chemical shifts of the *meta* carbons (C6b, C4b) and the *ipso* carbon (C8b) in mono1 F-FF as well as those of the *meta* carbons (C4a, C6a) and the *ipso* carbon (C8a) in mono2 F-FF are more downfield than they are in di F-FF.

In analogy, the most deshielded positions are the *ortho* and *para* positions in the fluorinated benzene ring. So, the most downfield signals in di F-FF are caused by the two C3 and two C5 atoms. The chemical shifts of these carbons in non-fluorinated phenylalanine moiety are more upfield, and that is the reason for the upfield shift of the signals of the *ortho* carbons (C3b, C7b) and of the *para* carbon (C5b) in mono1 F-FF, and of the signals of the *ortho* carbons (C3a, C7a) and of the *para* carbon (C5a) in mono2 F-FF.

5. CONFORMATIONAL PREFERENCE FOR THE NH−CH BOND

5.1. NH−CHb Rotamers and Specific Solvation. We computed the rotational profiles of the NH−CHb bond for FF, mono1 F-FF, mono2 F-FF, and di F-FF. Beginning with the conformation found in the crystal structure of the parent compound FF,[16] we determined the rotational profile by driving the τ = ∠(C−N−C−CO_2) dihedral angle, and rotational profiles were determined in each case for the dipeptide itself and the aggregate formed with one specific solvation water. The resulting rotational profiles are shown in Figure 5 for the four systems. The molecular models of the NH−CHb bond conformers are shown in Figures 6 and 7 for the parent FF

https://doi.org/10.1021/acsomega.2c06351
ACS Omega 2022, 7, 42629−42643

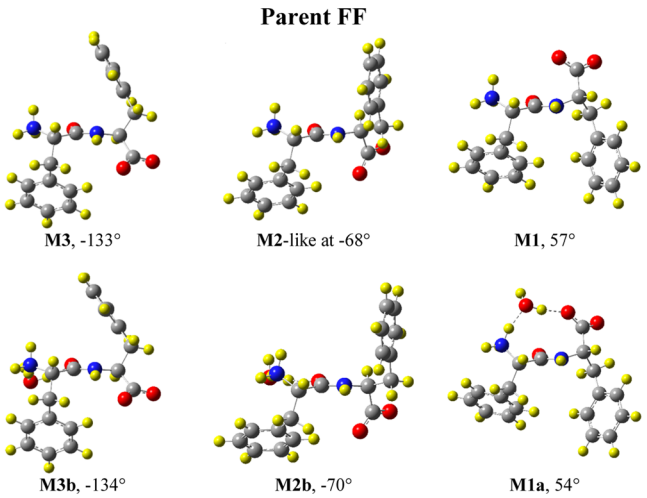

Figure 6. Minima of parent FF. In each case, the unbridged structures are shown on top and the bridged structures are on bottom. See text for an explanation of nomenclature.

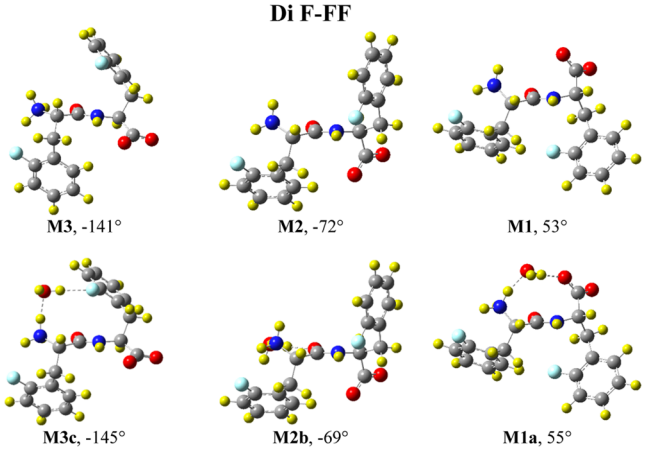

Figure 7. Minima of parent di F-FF. In each case, the unbridged structures are shown on top and the bridged structures are on bottom. See text for an explanation of nomenclature.

and di F-FF, respectively, and the molecular models of the conformers of the mono1 F-FF and the mono2 F-FF are provided in Figures S22 and S23. In the top and bottom rows of the figures, molecular models are shown of the conformer structures without and with specific solvation.

The conformations denoted as **M1** and **M1a** most closely resemble the ion pair structure found in the crystal structure of parent FF, and these two structures are necessary to quantify the stabilization afforded by the formation of the water-separated ion pair in crystals. While our focus is on **M1** and **M1a**, we recognize the possible formation of a contact ion pair **M1-CIP** and of neutral dipeptides **M1-N1**, **M1-N2**, and **M1-N3** and included the structures in the potential energy surface analyses for the parent diphenylalanine and the three fluorinated structures. Having localized **M1-CIP** for a given dipeptide, we then optimized **M1-N1**, the structure resulting by proton transfer from the ammonium group to the carboxylate group to form a neutral dipeptide with an $H_2N\cdots$HOCO hydrogen bond involving a *cis* carboxylic acid with $\angle$(H−O−C═O) ≈ 180°. In addition, we optimized local minima for the neutral structures **M1-N2** and **M1-N3** containing a *trans* carboxylic acid with $\angle$(H−O−C═O) ≈ 0° and with the potential for HNH··· HOCO or HNH···OCOH hydrogen bonding, respectively. Molecular models of these sets of four structures are shown in Figure S24a−d along with their relative energies ΔE and ΔG with respect to the most stable minimum **M3**. Cartesian coordinates of all stationary structures are collected in the Supporting Information.

Rotation about the NH−CHb bond is of the sp^2−sp^3 type, which features at most six idealized conformations **A**−**F** with τ = ±30, ±90, and ±150°, as shown in the top row of Scheme 4. In each of the conformations **A**−**F**, one substituent of the sp^3 carbon is placed perpendicular to the OC−NH plane. However, there are at most three minima **M1**−**M3** along the rotational profiles and they are schematically shown in the bottom row of Scheme 4. At least one of the large substituents is placed in the privileged position perpendicular to the OC−NH plane and hence structures **C** and **F** do not exist. Structure of type **E** does not exist because of the steric interference between the two Ph groups. Intramolecular nonbonded interactions (*vide infra*) cause substantial deviations of the τ values from the idealized conformations. In addition, the backbone nitrogen features a minor degree of pyramidalization, and we measured the improper dihedral angle φ = $\angle$(C−N−C−H(N)). The values of τ and φ of all of the minima are summarized in Table 3. The expected values of τ are shown in the parentheses and the expected values of φ are 180° if the N is flat. In the last row, we calculated the difference of the expected values and the actual values. In fact, in the case of the parent FF molecule and of mono1 F-FF, an **M2**-type structure does not exist as a local minimum and the **M2**-like structures shown in Figures 5 and S22 were computed at the fixed τ values given in the figures. The specific water solvent in **M1a** bridges between the NH_3^+ and the H-bond acceptor CO_2^-. In conformer **M2** and **M3**, more than one option for the aggregate formation may exist and those will be referred to as **b**- and **c**-types.

The rotational profile of FF is shown in Figure 5a as a dark blue dashed line and features two minima, **M1** (τ = 57°) and **M3** (τ = −133°) shown in the top row of Figure 6. Even though **M1** is the preferred conformation in the crystal structure, **M3** is 4.4 kcal mol^{-1} more stable than **M1**. The rotational profile of FF computed with an extra molecule of water included as a specific solvent molecule is more complicated because the solvation mode changes along the rotational profile. The conformation found in the crystal structure is perfectly set up for a water molecule to bridge the frustrated ion pair in minimum **M1a** (τ = 54°), that is, the water engages the H bond donor NH_3^+ and the H bond acceptor CO_2^- (**a**-type). Changes in the dihedral angle τ trace the light blue solid rotational profile of Figure 5a. In the region $\tau \approx 0°$ the distance between the NH_3^+ and the CO_2^- groups becomes too long for **a**-type water bridging, and the **b**-type of specific solvation starts to compete. In this **b**-type mode, the specific water molecule retains the stronger H bond to the NH_3^+ group and forms a second H bond with the carbonyl-O acceptor. The red solid rotational profile of Figure 5a is the segment where the **b**-type is preferred and contains minima **M2b** (τ = −70°) and **M3b** (τ = −134°). Molecular models of **M1a**, **M2b**, and **M3b** are shown in the bottom row of Figure 6.

The resulting rotational profiles of mono1 F-FF, mono2 F-FF, and di F-FF are similar and are shown in Figure 5b−d as dark blue dashed lines and features two (mono1 F-FF) or three minima (mono2 F-FF and di F-FF). Molecular models of these minima are shown in Figure 6 for di F-FF and Figures S19 and S20 for mono1 F-FF and mono2 F-FF, respectively. The

https://doi.org/10.1021/acsomega.2c06351
ACS Omega 2022, 7, 42629−42643

Scheme 4. Newman Projections of Idealized and Actual Conformations about the NH−CHb Bond

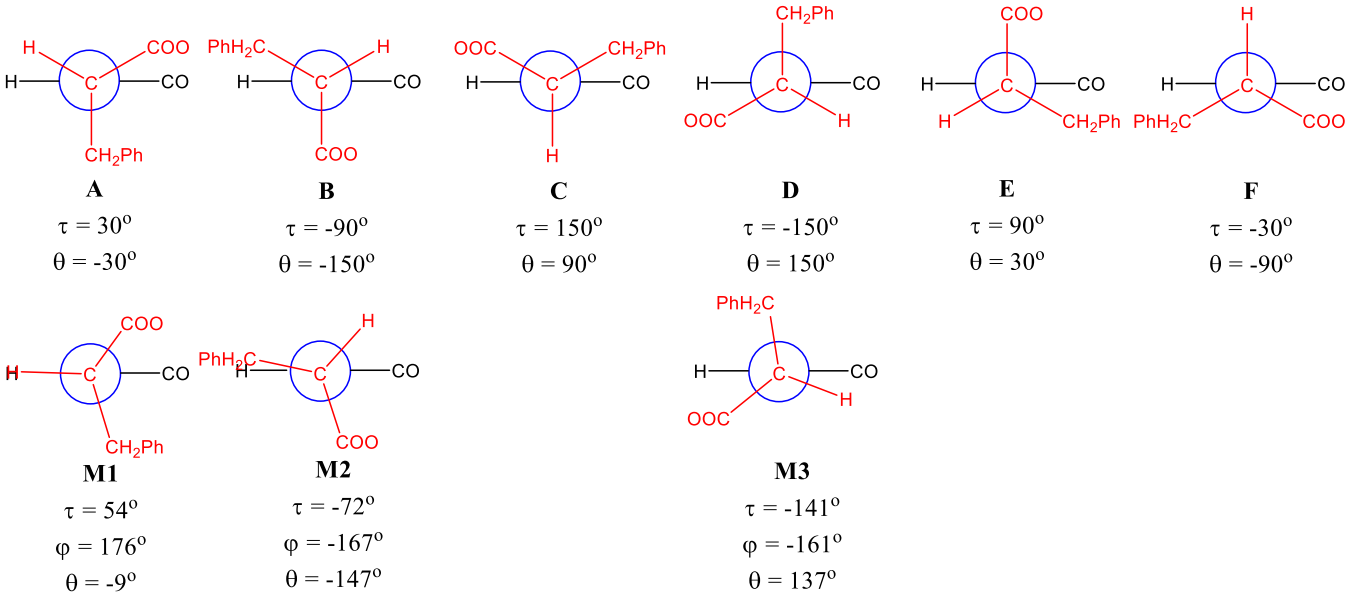

Table 3. Dihedral Angle of Minima along the Rotational Profile (°)

	M1 type		M2 type		M3 type	
	τ (30)	φ	τ (−90)	φ	τ (−150)	φ
FF	57	159			−133	−154
FF WB[a]	54	168	−70	−164	−134	−156
Mono1 F-FF	61	152			−139	−159
Mono1 F-FF WB	54	168	−73	−160	−135	−156
Mono2 F-FF	53	177	−73	−170	−134	−154
Mono2 F-FF WB	55	174	−72	−170	−140	−157
Di F-FF	54	176	−72	−167	−141	−161
Di F-FF WB	55	172	−69	−166	−146	−164
AD[b]	25	12	19	14	12	22

[a]WB: water bridge, referring to the structures with one solvent water. [b]AD: averaged difference from the expected value.

following structural discussion focuses on di F-FF and similar considerations apply to the mono-substituted species.

For di F-FF, while conformation **M1** (τ = 53.8°) is preferred in the crystal structure, minima **M2** (τ = −73.0°) and **M3** (τ = −141.1°) are more stable by 2.77 and 3.40 kcal mol^{-1}, respectively. Careful inspection of the rotational profile shows a discontinuity at $\tau \approx 90°$ because of a change in the preferred arene-arene interaction. The rotational profile of di F-FF computed with one molecule of water included as a specific solvent molecule is shown in solid lines in Figure 5d. The light blue demonstrates the conformation found in the crystal structure where the water engages the H bond donor NH_3^+ and the H bond acceptor CO_2^- (**a**-type) with the minimum **M1a** (τ = 55.4°). And the orange line represents the **b**-type mode where the specific water molecule retains the stronger H bond to the NH_3^+ group and forms a second H bond with the carbonyl-O acceptor, with the minima **M2b** (τ = −69.5°) and **M3b** (τ = −139.6°). The rotational profile includes a third coordination mode (**c**-type) with water bridging between the always engaged H-bond donor NH_3^+ and an F atom serving as a H-bond acceptor. This coordination mode is traced out by the green solid segment of the rotational profile, and it is preferred in the

Table 4. Conformational Preference Energies[a]

	with specific water solvation				without specific water solvation			
molecule	ΔE	ΔG	K^b	CPR[c]	molecule	ΔE	ΔG	K^b
				FF				
M2bν.**M1a**	2.19	2.63	0.01	84.5				
M3cν.**M1a**	1.26	1.65	0.06	16.2	**M3** vs **M1**	−4.45	−5.07	5180
				Mono1 F-FF				
M2bν.**M1a**	1.12	1.23	0.13	8.0				
M3cν.**M1a**	0.38	1.00	0.19	5.4	**M3** vs **M1**	−4.68	−4.35	1538
				Mono2 F-FF				
M2bν.**M1a**	1.84	2.29	0.02	47.6	**M2** vs **M1**	−2.79	−3.60	434
M3cν.**M1a**	0.81	−0.46	2.17	0.5	**M3** vs **M1**	−3.15	−5.10	5449
				Di F-FF				
M2bν.**M1a**	2.15	1.99	0.03	28.7	**M2** vs **M1**	−2.77	−3.08	180
M3cν.**M1a**	0.96	−1.32	9.27	0.1	**M3** vs **M1**	−3.41	−3.21	225

[a]Relative energies in kcal mol^{-1}. [b]Equilibrium constant K for **M1** type → **Mx** type computed with $\Delta G = -RT\cdot\ln(K)$ at room temperature. [c]Conformational preference ratio (CPR) = $1/K$ = [**M1** type]/[**Mx** type].

https://doi.org/10.1021/acsomega.2c06351
ACS Omega 2022, 7, 42629−42643

Table 5. Hydration Energies of Conformers of FF and Fluorinated Derivatives at SMD(B3LYP/6-31G*)

molecule	ΔE_{water} [a]	ΔG_{water} [a]	$\Delta^W A_{water}$ [a]	K_{water} [b]	BR [c]
			FF		
M1 + H_2O → **M1a**	−14.11	−3.26	−5.43	9507.66	522921.11
M3 + H_2O → **M3b**	−8.40	3.45	1.29	0.11	6.24
			Mono1 F-FF		
M1 + H_2O → **M1a**	−13.94	−1.93	−4.1	1008.56	55470.82
M3 + H_2O → **M3b**	−8.90	3.42	1.25	0.12	6.68
			Mono2 F-FF		
M1 + H_2O → **M1a**	−14.60	−3.20	−5.37	8592.45	472584.59
M2 + H_2O → **M2b**	−9.96	2.68	0.51	0.42	23.27
M3 + H_2O → **M3c**	−9.51	2.88	0.70	0.31	16.89
			Di F-FF		
M1 + H_2O → **M1a**	−14.56	−1.67	−3.85	661.53	36384.13
M2 + H_2O → **M2b**	−9.65	3.39	1.22	0.13	7.03
M3 + H_2O → **M3c**	−10.19	0.22	−1.95	26.96	1482.55

[a]Hydration energies in kcal mol^{-1}. [b]Equilibrium constant K_{water} computed with $\Delta^W A_{water} = -RT\cdot\ln(K_{water})$ at room temperature. [c]Bridging ratio BR = [bridged]/[unbridged] computed as product $K_{water}\cdot[H_2O]$.

region $\tau \approx -95$ to $-180°$. Minimum **M3c** ($\tau = -145.6°$, Figure 6) is 1.39 kcal mol^{-1} more stable than **M3b**.

The rotational profiles of Figure 5 demonstrate that the water-bridged ion pair **M1a** is greatly stabilized compared to the unbridged structure **M1**, and this is true for all four diphenylalanines. Conformational preference energies ΔE and ΔG are listed in Table 4 with and without the specific water solvation. While the conformational preference energies ΔE would suggest the **M1a** structure to be the most stable conformation for all four diphenylalanines, the ΔG values indicated that the **M3c** structures are preferred for mono2 F-FF ($\Delta G = -0.5$ kcal mol^{-1}) and di F-FF ($\Delta G = -1.32$ kcal mol^{-1}).

Our finding of the water-bridged structure **M1a** being the most stable structure of the parent diphenylalanine resolves the apparent discrepancy between the known conformation of the water-bridged FF in its crystal structure, and the solution structure **M1** of FF. Moreover, our results suggest that the conformation of the water-bridged FF in the crystal structure is not caused by crystal packing, but rather that the crystal structure is the result of preorganization of the solution structure by specific solvation.

The ΔG values for the conformational energy allow for the calculation of the equilibrium constants K = [**Mx** type]/[**M1** type] (Table 4). Note that the K values for the structures without specific water solvation are in the hundreds or thousands, while the K values of structures with specific water solvation are magnitudes lower, which indicates that the competitiveness of **M1**-type structures is because of the specific water solvation. We also list in Table 4 the conformational preference ratio (CPR) for the **M1**-type structures, which are simply the reciprocal values of K; CPR = $1/K$ = [**M1** type]/[**Mx** type]. The CPR values show a decline of relative **M1a** concentration with fluorination and this decline is most pronounced for mono2 F-FF and di F-FF. If preorganization of the solution structure by specific solvation is needed for crystallization of the type observed for FF, the chances to crystallize mono1 F-FF are at least 10-fold higher compared to the other fluorinated diphenylalanines.

These calculations suggest that water bridging can change the preferred conformation in solution. And they also provide an explanation why crystals of fluorinated FF are very difficult to obtain. In FF, it is obvious that **M1** with water bridging is the dominant structure compared to **M2** and **M3** types. We have studied water bridging in other contexts extensively[47−49] and found that the engagement of the bridging water molecule in two hydrogen-bonding interactions synergistically enhances both. Therefore, one has every reason to assume that the bridging water molecule would be present in clusters of **M1** with more specific water molecules.

In Table 5, we report on the thermochemistry of several hydration reactions. If a conformation occurs without and with specific water solvation, we computed the hydration energy for the molecule in that conformation. The conformations **M1** and **M1a** most closely resemble the ion pair structure found in the crystal structure of parent FF and the energy of the reaction **M1** + H_2O → **M1a** quantifies the stabilization due to the formation of the water-separated ion pair in the conformation that occurs in the crystal. We report ΔE_{water}, ΔG_{water}, and $\Delta^W A_{water}$ to estimate the water binding energy. While the ΔG values are appropriate for discussion of conformational preference (because pV terms cancel), the accurate determination of hydration energies requires $\Delta^W A_{water}$ to properly account for translational entropy changes in solution and the absence of significant volume effects in solution. With the $\Delta^W A_{water}$ values, we computed the equilibrium constant K_{water} for the water adduct formation and the bridging ratio BR = [bridged]/[unbridged].

In the context of crystal engineering fluorinated derivatives of diphenylalanine, the bridging ratio BR = [**M1a**]/[**M1**] is the most relevant because it quantifies the advantage for conformer **M1a** provided by specific solvation. The BR values in Table 5 clearly show that the water-bridged **M1a** structure dominates by more than 99% over **M1**. For corroboration, we optimized all **M1** and **M1a** structures at the correlated level SMD(MP2/6-31G*), their molecular models are shown in Figure S25 to be very similar to their SMD(B3LYP/6-31G*) structures, and the thermochemistry for the reaction **M1** + H_2O → **M1a** at the correlated level confirms our conclusion.

5.2. Coupling Constant J_{NH-CH} as a Function of Dihedral Angle. It is clear that the computed NMR properties for any one minimum structure will not match the measured NMR data. Instead, fast rotations about the HN−CH, HC−CH_2Ph, and CH_2−Ph bonds occur, and the measured NMR data contain information about these dynamic processes. The structures-NMR relationship is nontrivial and requires mathematical approaches to deduce the best match of the NMR data

https://doi.org/10.1021/acsomega.2c06351
ACS Omega 2022, 7, 42629−42643

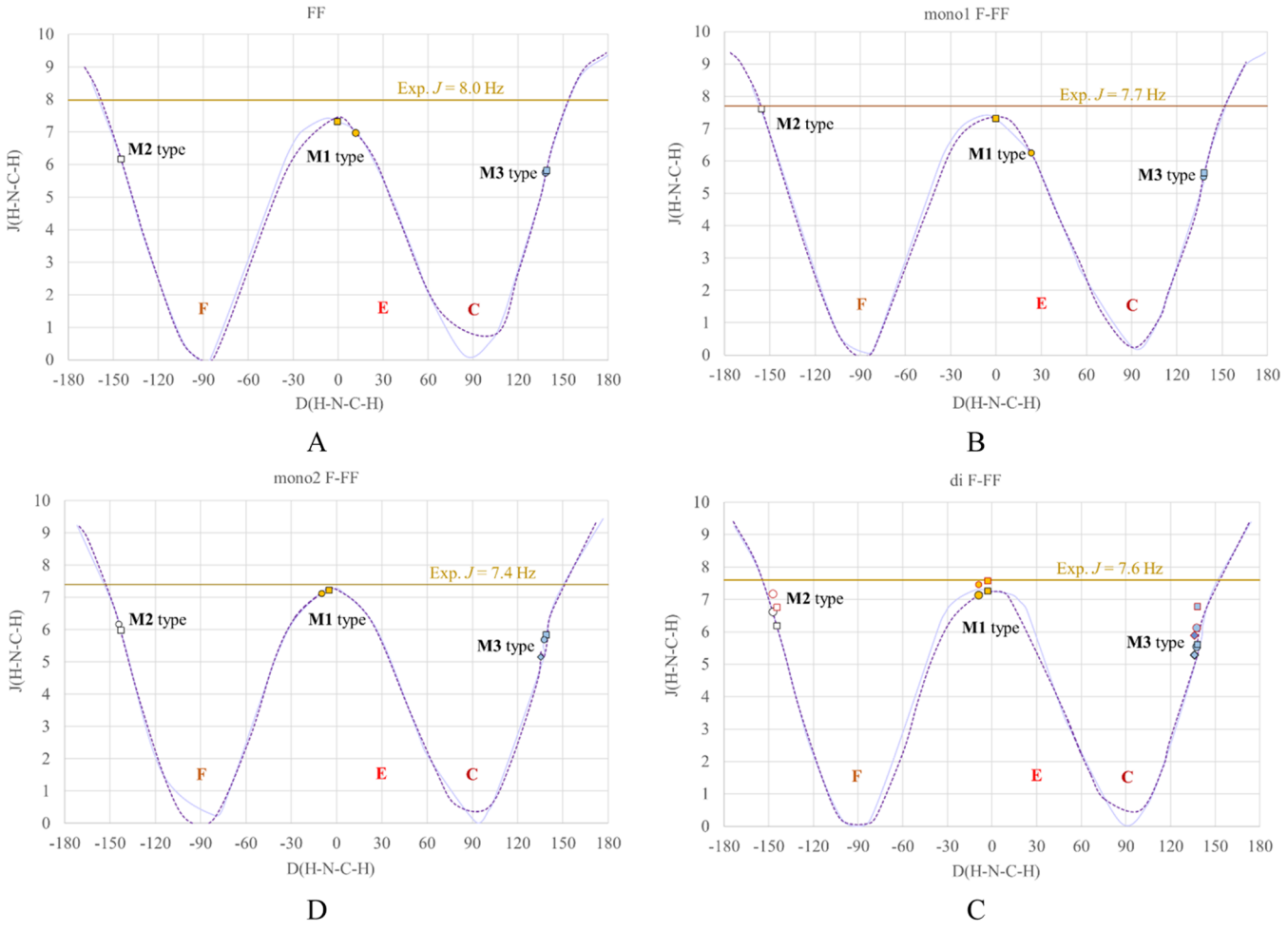

Figure 8. Karplus relationship of dihedral angle ∠(H−N−C−H) for FF (A), mono1 F-FF (B), mono2 F-FF (C), and di F-FF (D) without (dark purple dashed line) and with (light purple solid line) water bridging computed at the SMD(B3LYP/6-31G*) level. Yellow markers: **M1**-type minima. White markers: **M2**-type minima. Blue markers: **M3**-type minima. Square markers: minima with water bridging. Round markers: minima without water bridging. Diamond markers: **M3c** minima.

and the solution structure(s), and such a study is in progress. One important aspect of the theoretical analysis of the NMR properties concerns the question regarding the relationship between the measured ^3J coupling constants and the NH−CHb rotational profiles and whether the Karplus curves can be used to distinguish between possible conformations.

After the study of the rotational profile clarified the relationship between the energy and $\tau = \angle(\mathrm{C{-}N{-}C{-}CO_2})$, we then explored the NMR properties related to this dihedral angle. The dihedral angle $\theta = \angle((\mathrm{N})\mathrm{H{-}N{-}C{-}Hb1})$ also describes the rotation along the same N−C bond, but with focus on the two hydrogen atoms, which have measurable coupling constants ^3J, which are related to the dihedral angle θ via the Karplus equation $J(\theta) = A\cos^2(\theta) + B\cos(\theta) + C$. Thus, we calculated the NMR chemical shifts and spin−spin coupling constants of all of the structures along the rotational profiles for all four structures (compare marks in Figure 5) and plotted their $^3J(\theta)$ against θ in Figure 8. Dark purple dashed lines were computed for the structures without water bridging and light purple solid lines refer to the structures with water bridging. Horizontal lines are included to indicate the measured ^3J values for each dipeptide from our own measurements (fluorinated dipeptides) and from the literature (parent FF).[50] Furthermore, the minima are shown in yellow (**M1** type), white (**M2** type), and blue (**M3** type) markers. It is well known that the ^3J values are theoretical level dependent[51] and for di F-FF, we also calculated the J values with a better basis set at the level of SMD(B3LYP/6-311+G(2d,p))//SMD(B3LYP/6-31G*). The results are marked in Figure 8d (markers with red frame) and show an increase of the J values for all minima and further improvements in the theoretical level might result in still higher J values. Our focus is less on the absolute J values, but we are interested in the relative J values and their relation to conformation.

Figure 8 shows the expected slightly asymmetric double-well curve for values $-180 \le \theta \le 180°$ with a large variation of $0 \le J(\theta) \le 10$ Hz. The minima of the Karplus curves occur for structures with conformations **C** ($\theta = 90°$) and **F** ($\theta = -90°$), see Scheme 4, and we have shown that the conformers with H(C) in the privileged position are not stationary structures. Putative structures with conformation **E** would be expected with θ values of about 30°, and they also do not exist as local minima on the potential energy surface. As can be seen in Figure 8, the calculated J values of stationary structures **M1** to **M3** fall within a narrow range of 2 Hz and therefore, J values do not inform about the conformation.

https://doi.org/10.1021/acsomega.2c06351
ACS Omega 2022, 7, 42629−42643

6. CONCLUSIONS

The three fluorinated diphenylalanines were synthesized by solid-phase peptide synthesis, purified by flash chromatography, and dipeptide purity and identity were established by LC−MS analysis. The pure dipeptides were studied in detail in partially deuterated aqueous solution with one- and two-dimensional NMR spectroscopic techniques. The results of the extensive NMR study include the unambiguous assignments of all chemical shifts for the H and C atoms of the aliphatic backbone (*a*-CH, *b*-CH, NH, *a*-CH_2, *b*-CH_2) and the complete assignments of all chemical shifts of the C atoms of the carboxylate, the amide carbonyl, the CF carbons, and of every arene C atom in each phenyl ring. In addition, the measurements allow for unambiguous determination of several H,H coupling constants ($^3J_{NH-CH}$, $^2J_{H-H}(CH_2)$, and $^3J_{b\text{-}CH\text{-}b\text{-}CH_2}$) and C,F coupling constants ($^1J_{C-F}$, both $^2J_{C-F}$ for every fluorinated phenyl group). The aromatic Hs cannot be assigned based on the ^{1}H NMR measurements alone; additional information would be required, for example, based on simulations of the observed splitting patterns. This highlights the significance of the C NMR measurements to inform about the environments of both arenes.

The NMR analysis clearly shows one set of signals for each dipeptide. This finding does not imply that each peptide adopts only one structure and the computed NMR properties for any minimum structure is not expected to match the measured NMR data. Instead, fast rotations about the NH−CH bond and as well as the HC−CH_2Ph and CH_2−Ph bonds occur and required the exploration of the NH−CH rotational profiles for FF and its fluorinated derivatives with the computational studies at the SMD(B3LYP/6-31G*) level. The rotational profiles were computed for the dipeptide themselves and for the aggregates formed by specific water solvation. Rotation about the NH−CHb bond is of the sp^2−sp^3 type and allows in principle for six conformations (**A**−**F**), and our results show that at most three conformational structures (**A**, **B**, and **D**) correspond to stationary structures (**M1**, **M2**, and **M3**).

The construction of the rotational profiles allowed for the computation of the associated Karplus curves for $^3J_{NHCH}$ using the GIAO method and they show the expected asymmetric double-well shape. The Karplus curves demonstrate similar *J* values for all computed stationary structures and do not allow any discrimination of conformational preferences. However, the analysis of the relative energies ΔE and ΔG of the stationary structures informs about the conformations. In the absence of specific solvation, the stability of the stationary structure follows the order **M3** > **M2** ≫ **M1**. In a stunning reversal of relative conformer stabilities, the specific water solvation makes all of the difference and adds a large competitive advantage to the water-separated ion pair **M1a**. In fact, **M1a** becomes the most stable and dominant conformation for the parent diphenylalanine and mono1 F-FF and **M1a** becomes competitive with **M3c** for mono2 F-FF and di F-FF.

It is only with the inclusion of the specific solvation that the conformation found in crystals of FF becomes a competitive structure in solution, and this finding suggests that such preorganization in solution might be an important factor in the crystallization of FF. If this hypothesis holds, the chances to crystallize mono1 F-FF are at least 10-fold higher compared to the other fluorinated diphenylalanines.

■ ASSOCIATED CONTENT

Supporting Information

The Supporting Information is available free of charge at https://pubs.acs.org/doi/10.1021/acsomega.2c06351.

Chromatogram and MS spectra, H NMR, C NMR, F NMR, TOCSY, HSQC, and HMBC spectra of each fluorinated diphenylalanine; energies and thermochemistry data of the stationary structures of FF and the fluorinated derivatives; molecular models of stationary structure of mono-fluorinated diphenylalanines; molecular models of the stationary structure of the **M1-CIP**, **M1-N1**, **M1-N2**, and **M1-N3**; molecular model of MP2 optimized **M1** and **M1a** structures; and Cartesian coordinates of all stationary structures (PDF)

■ AUTHOR INFORMATION

Corresponding Author

Rainer Glaser − *Department of Chemistry, Missouri University of Science and Technology, Rolla, Missouri 65409, United States*; orcid.org/0000-0003-3673-3858; Email: GlaserR@umsystem.edu

Authors

Kaidi Yang − *Department of Chemistry, University of Missouri, Columbia, Missouri 65211, United States*

Fabio Gallazzi − *Department of Chemistry and Molecular Interactions Core, University of Missouri, Columbia, Missouri 65211, United States*

Christina Arens − *Department of Chemistry, Missouri University of Science and Technology, Rolla, Missouri 65409, United States*

Complete contact information is available at: https://pubs.acs.org/10.1021/acsomega.2c06351

Notes

The authors declare no competing financial interest.

■ ACKNOWLEDGMENTS

This research was supported by the Missouri University of Science and Technology and, in part, by NSF grant #1665487. C.A. gratefully acknowledges support by an OURE scholarship. The authors thank Brian Jameson for measuring F NMR spectra.

■ REFERENCES

(1) Ganeev, R. A.*Nonlinear Optical Properties of Materials*; Springer: New York, 2013.

(2) Garmire, E. Nonlinear Optics in Daily Life. *Opt. Express* **2013**, *21*, 30532−30544.

(3) Franken, P. A.; Hill, A. E.; Peters, C. W.; Weinreich, G. Generation of Optical Harmonics. *Phys. Rev. Lett.* **1961**, *7*, 118−120.

(4) Bloembergen, N.; Pershan, P. S. Light Waves at the Boundary of Nonlinear Media. *Phys. Rev.* **1962**, *128*, 606−621.

(5) Boyd, R.The Nonlinear Optical Susceptibility. In *Nonlinear Optics*, 3rd ed.; Academic Press: Cambridge, MA, 2007; pp 1−67.

(6) Ray, P. C. Size. and Shape Dependent Second Order Nonlinear Optical Properties of Nanomaterials and Its Application in Biological and Chemical Sensing. *Chem. Rev.* **2010**, *110*, 5332−5365.

(7) Marder, S. R. Organic Nonlinear Optical Materials: Where We Have Been and Where We Are Going. *Chem. Commun.* **2006**, 131−134.

(8) Bosshard, Ch.; Sutter, K.; Pretre, P.; Hulliger, J.; Florsheimer, M.; Kaatz, P.; Gunter, P.*Organic Nonlinear Optical Materials*; Bordon and Breach Publishers: Basel, Switzerland, 2020.

(9) Glaser, R. Polar Order By Rational Design: Crystal Engineering With Parallel Beloamphiphile Monolayers. *Acc. Chem. Res.* **2007**, *40*, 9−17.
(10) Bhoday, H.; Lewis, M.; Kelley, S. P.; Glaser, R. Perfect Polar Alignment of Parallel Beloamphiphile Monolayers: Synthesis, Characterization, and Crystal Architectures of Unsymmetrical Phenoxy-Substituted Acetophenone Azines. *ChemPlusChem* **2022**, *87*, No. e202200224.
(11) *Nonlinear Systems, Vol. 2: Nonlinear Phenomena in Biology, Optics and Condensed Matter*, Archilla, J. F. R.; Palmero, F.; Lemos, M. C.; Sanchez-Rey, B.; Casado-Pascual, J., Eds.; Springer: New York, NY, 2018.
(12) Duboisset, J.; Deiset-Besseau, A.; Benichou, E.; Russier-Antoine, I.; Lascoux, N.; Jonin, C.; Hache, F.; Schanne-Klein, M.; Brevet, P. A Bottom-Up Approach to Build the Hyperpolarizability of Peptides and Proteins from their Amino Acids. *J. Phys. Chem. B* **2013**, *117*, 9877−9881.
(13) Uma, B.; Rajnikant; Murugesand, K. S.; Krishnan, S.; Boaz, B. M. Growth, Structural, Optical, Thermal and Dielectric Properties of A Novel Semi-Organic Nonlinear Optical Crystal: Dichloro-Diglycine Zinc II. *Prog. Nat. Sci.: Mater. Int.* **2014**, *24*, 378−387.
(14) Glaser, R.; Kaszynski, P.*Anisotropic Organic Materials: Approaches to Polar Order*; American Chemical Society: Washington, DC, 2011.
(15) Glaser, R.; Knotts, N.; Yu, P.; Li, L.; Chandrasekhar, M.; Martin, C.; Barnes, C. L. Perfect Polar Stacking of Parallel Beloamphiphile Layers. Synthesis, Structure, and Solid-State Optical Properties of the Unsymmetrical Acetophenone Azine DCA. *Dalton Trans.* **2006**, 2891−2899.
(16) Gorbitz, C. H. Nanotube Formation by Hydrophobic Dipeptides. *Chem. - Eur. J.* **2001**, *7*, 5153−5159.
(17) Marchesan, S.; Vargiu, A. V.; Styan, K. E. The Phe-Phe Motif for Peptide Self-Assembly in Nanomedicine. *Molecules* **2015**, *20*, 19775−19788.
(18) Li, Q.; Jia, Y.; Dai, L.; Yang, Y.; Li, J. Controlled Rod Nanostructured Assembly of Diphenylalanine and Their Optical Waveguide Properties. *ACS Nano* **2015**, *9*, 2689−2695.
(19) Porter, S. L.; Coulter, S. M.; Pentlavalli, S.; Thompson, T. P.; Laverty, G. Self-Assembling Diphenylalanine Peptide Nanotubes Selectively Eradicate Bacterial Biofilm Infection. *Acta Biomater.* **2018**, *77*, 96−105.
(20) Guo, L.; Yang, B.; Wu, D.; Tao, Y.; Kong, Y. Chiral Sensing Platform Based on the Self-Assemblies of Diphenylalanine and Oxalic Acid. *Anal. Chem.* **2018**, *90*, 5451−5458.
(21) Reches, M.; Gazit, E. Casting Metal Nanowires within Discrete Self-Assembled Peptide Nanotubes. *Science* **2003**, *300*, 625−627.
(22) Huang, S.; Chen, G.; Ou, R.; Qin, S.; Wang, F.; Zhu, F.; Ouyang, G. Ultrathin Self-Assembled Diphenylalanine Nanosheets through a Gold-Stablilized Strategy for High-Efficiency Adsorption/Desorption/Ionization. *Anal. Chem.* **2018**, *90*, 8607−8615.
(23) Selvarani, K.; Mahalakshmi, R. A Review on Physical and Chemical Properties of L-Phenylalanine Family of NLO Single Crystals. *Int. J. Chem. Tech. Res.* **2016**, *9*, 113−120.
(24) Pizzi, A.; Catalano, L.; Demitri, N.; Dichiarante, V.; Terraneo, G.; Metrangolo, P. Halogen Bonding as a Key Interaction in the Self-Assembly of Iodinated Diphenylalanine Peptides. *Pept. Sci.* **2020**, *112*, No. e24127.
(25) Khanra, S.; Cipriano, T.; Lam, T.; White, T. A.; Fileti, E. E.; Alves, W. A.; Guha, S. Self-Assembled Peptide−Polyfluorene Nanocomposites for Biodegradable Organic Electronics. *Adv. Mater. Interfaces* **2015**, *2*, No. 1500265.
(26) Khanra, S.; Vassiliades, S.; Alves, W.; Yang, K.; Glaser, R.; Ghosh, K.; Bhattacharya, P.; Yu, P.; Guha, S. Enhanced Piezo Response and Nonlinear Optical Properties of Fluorinated Self-Assembled Peptide Nanotubes. *AIP Adv.* **2019**, *9*, 115202−115206.
(27) Keeler, J.*Understanding NMR Spectroscopy*, 2nd ed.; Wiley: Hoboken, NJ, 2010; pp 221−225.
(28) Ibid., 209−210.
(29) Ibid., 215−219.
(30) Ibid., 281−284.
(31) Petersson, G. A.; Bennett, A.; Tensfeldt, T. G.; Al-Laham, M. A.; Shirley, W. A.; Mantzaris, J. A complete basis set model chemistry. I. The total energies of closed-shell atoms and hydrides of the first-row atoms. *J. Chem. Phys.* **1988**, *89*, 2193−218.
(32) Marenich, A. V.; Cramer, C. J.; Truhlar, D. G. Universal solvation model based on solute electron density and a continuum model of the solvent defined by the bulk dielectric constant and atomic surface tensions. *J. Phys. Chem. B* **2009**, *113*, 6378−96.
(33) Glaser, R.; Yin, J.; Miller, S. Asymmetry in the *N*-Inversion of Heteroarene Imines: Pyrimidin-4(3*H*)-Imine, Pyridin-2(1*H*)-Imine, and 1H-Purine-6(9*H*)-Imine. *J. Org. Chem.* **2010**, *75*, 1132−1142.
(34) Coyle, S.; Glaser, R. Asymmetric Imine *N*-Inversion in 3-Methyl-4-Pyrimidinimine. Molecular Dipole Analysis of Solvation Effects. *J. Org. Chem.* **2011**, *76*, 3987−3996.
(35) Krishnan, R.; Binkley, J. S.; Seeger, R.; Pople, J. A. Self-Consistent Molecular Orbital Methods. XX. A Basis Set for Correlated Wave Functions. *J. Chem. Phys.* **1980**, *72*, 650−654.
(36) London, F. The quantic theory of inter-atomic currents in aromatic combinations. *J. Phys. Radium* **1937**, *8*, 397−409.
(37) Helgaker, T.; Watson, M.; Handy, N. C. Analytical calculation of nuclear magnetic resonance indirect spin-spin coupling constants at the generalized gradient approximation and hybrid levels of density-functional theory. *J. Chem. Phys.* **2000**, *113*, 9402−09.
(38) Møller, C.; Plesset, M. S. Note on an approximation treatment for many-electron systems. *Phys. Rev.* **1934**, *46*, 0618−22.
(39) Frisch, M. J.; Head-Gordon, M.; Pople, J. A. Direct MP2 gradient method. *Chem. Phys. Lett.* **1990**, *166*, 275−80.
(40) Frisch, M. J.; Trucks, G. W.; Schlegel, H. B.; Scuseria, G. E.; Robb, M. A.; Cheeseman, J. R.; Scalmani, G.; Barone, V.; Petersson, G. A.; Nakatsuji, H.; Li, X.; Caricato, M.; Marenich, A. V.; Bloino, J.; Janesko, B. G.; Gomperts, R.; Mennucci, B.; Hratchian, H. P.; Ortiz, J. V.; Izmaylov, A. F.; Sonnenberg, J. L.; Williams-Young, D.; Ding, F.; Lipparini, F.; Egidi, F.; Goings, J.; Peng, B.; Petrone, A.; Henderson, T.; Ranasinghe, D.; Zakrzewski, V. G.; Gao, J.; Rega, N.; Zheng, G.; Liang, W.; Hada, M.; Ehara, M.; Toyota, K.; Fukuda, R.; Hasegawa, J.; Ishida, M.; Nakajima, T.; Honda, Y.; Kitao, O.; Nakai, H.; Vreven, T.; Throssell, K.; Montgomery, J. A., Jr.; Peralta, J. E.; Ogliaro, F.; Bearpark, M. J.; Heyd, J. J.; Brothers, E. N.; Kudin, K. N.; Staroverov, V. N.; Keith, T. A.; Kobayashi, R.; Normand, J.; Raghavachari, K.; Rendell, A. P.; Burant, J. C.; Iyengar, S. S.; Tomasi, J.; Cossi, M.; Millam, J. M.; Klene, M.; Adamo, C.; Cammi, R.; Ochterski, J. W.; Martin, R. L.; Morokuma, K.; Farkas, O.; Foresman, J. B.; Fox, D. J.; et al.*Gaussian 09*; Gaussian, Inc.: Wallingford, CT, 2016.
(41) Wertz, D. H. Relationship Between the Gas-phase Entropies of Molecules and their Entropies of Solvation in Water and 1-Octanol. *J. Am. Chem. Soc.* **1980**, *102*, 5316−5322.
(42) Coupling constants, NMR Facility: US San Diego, 2022. http://sopnmr.ucsd.edu/coupling.htm.
(43) Hoye, T. R.; Zhao, H. A Method for Easily Determining Coupling Constant Values: An Addendum to "A Practical Guide to First-Order Multiplet Analysis in ^{1}H NMR Spectroscopy". *J. Org. Chem.* **2002**, *67*, 4014−4016.
(44) Nikolova, V.; Cheshmedzhieva, D.; Ilieva, S.; Galabov, B. Atomic Charges in Describing Properties of Aromatic Molecules. *J. Org. Chem.* **2019**, *84*, 1908−1915.
(45) Spectral Database for Organic Compounds (SDBS); 1H-NMR; SDBS No.: 1165; HSP-49-525, 2022. https://sdbs.db.aist.go.jp/sdbs/cgi-bin/direct_frame_top.cgi.
(46) Spectral Database for Organic Compounds (SDBS); 13C-NMR; SDBS No.: 11156; CDS-13-369, 2022. https://sdbs.db.aist.go.jp/sdbs/cgi-bin/direct_frame_top.cgi.
(47) Lewis, M.; Glaser, R. Synergism of Catalysis and Reaction Center Rehybridization. An ab Initio Study of the Hydrolysis of the Parent Carbodiimide. *J. Am. Chem. Soc.* **1998**, *120*, 8541−8542.
(48) Lewis, M.; Glaser, R. Synergism of Catalysis and Reaction Center Rehybridization in Nucleophilic Additions to Cumulenes: The One-, Two- and Three-Water Hydrolyses of Carbodiimide and Methyleneimine. *Chem. - Eur. J.* **2002**, *8*, 1934−1944.

https://doi.org/10.1021/acsomega.2c06351
ACS Omega 2022, 7, 42629−42643

(49) Lewis, M.; Glaser, R. Synergism of Catalysis and Reaction Center Rehybridization. A Novel Mode of Catalysis in the Hydrolysis of Carbon Dioxide. *J. Phys. Chem. A* **2003**, *107*, 6814−6818.
(50) Chu, Y. H.; Wang, K. T. ^{1}H NMR Spectra of Diastereomeric Aromatic Dipeptides (Phe-Phe) in Aqueous Solution. *Magn. Reson. Chem.* **1985**, *23*, 450−453.
(51) Jensen, F. The Basis Set Convergence of Spin−Spin Coupling Constants Calculated by Density Functional Methods. *J. Chem. Theory Comput.* **2006**, *2*, 1360−1369.

https://doi.org/10.1021/acsomega.2c06351
ACS Omega 2022, 7, 42629−42643